

See discussions, stats, and author profiles for this publication at: <https://www.researchgate.net/publication/264201107>

Correlating Particle Deformation with Water Concentration Profiles during Latex Film Formation: Reasons That Softer Latex Films Take Longer to Dry

ARTICLE *in* LANGMUIR · JULY 2014

Impact Factor: 4.46 · DOI: 10.1021/la5023505 · Source: PubMed

CITATIONS

6

READS

135

5 AUTHORS, INCLUDING:



Farai Carter

University of Surrey

1 PUBLICATION 6 CITATIONS

[SEE PROFILE](#)



Radoslaw M Kowalczyk

University of Reading

28 PUBLICATIONS 327 CITATIONS

[SEE PROFILE](#)



Joseph Keddie

University of Surrey

147 PUBLICATIONS 3,832 CITATIONS

[SEE PROFILE](#)

Correlating Particle Deformation with Water Concentration Profiles during Latex Film Formation: Reasons That Softer Latex Films Take Longer to Dry

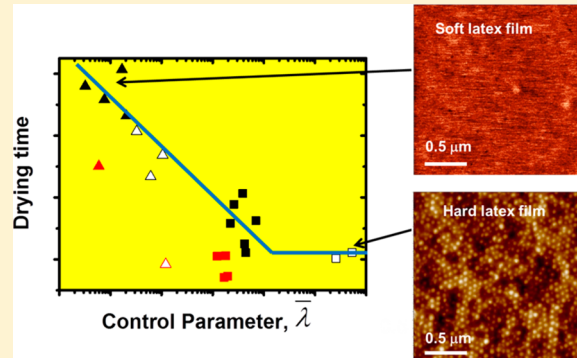
Farai T. Carter,[†] Radoslaw M. Kowalczyk,[†] Ian Millichamp,[‡] Malcolm Chainey,[‡] and Joseph L. Keddie*,[†]

[†]Department of Physics, Faculty of Engineering and Physical Sciences, University of Surrey, Guildford, Surrey, GU2 7XH United Kingdom

[‡]AkzoNobel International Paint Ltd, Stoneygate Lane, Felling, Gateshead, Tyne and Wear, NE10 0JY United Kingdom

S Supporting Information

ABSTRACT: During the past two decades, an improved understanding of the operative particle deformation mechanisms during latex film formation has been gained. For a particular colloidal dispersion, the Routh–Russel deformation maps predict the dominant mechanism for particle deformation under a particular set of conditions (evaporation rate, temperature, and initial film thickness). Although qualitative tests of the Routh–Russel model have been reported previously, a systematic study of the relationship between the film-formation conditions and the resulting water concentration profiles is lacking. Here, the water distributions during the film formation of a series of acrylic copolymer latexes with varying glass-transition temperatures, T_g (values of -22 , -11 , 4 , and 19 °C), have been obtained using GARField nuclear magnetic resonance profiling. A significant reduction in the rate of water loss from the latex copolymer with the lowest T_g was found, which is explained by its relatively low polymer viscosity enabling the growth of a coalesced skin layer. The set of processing parameters where the drying first becomes impeded occurs at the boundary between the capillary deformation and the wet sintering regimes of the Routh–Russel model, which provides strong confirmation of the model's validity. An inverse correlation between the model's dimensionless control parameter and the dimensionless drying time is discovered, which is useful for the design of fast-drying waterborne films.



INTRODUCTION

The formation of a dry, homogeneous film from a dispersion of colloidal polymer particles in water is described as a series of three sequential processes.^{1–3} These processes are (1) the evaporation of water to concentrate the particles and overcome the repulsion that maintains colloidal stability,⁴ (2) the deformation of the polymer particles into space-filling polyhedra,^{5–8} and (3) the interdiffusion of the polymer chains to blur the particle boundaries and to build cohesive strength.^{9–12} Numerous experimental studies have traced the structural evolution from dispersed polymer particles in water to a dry, coalesced, homogeneous film on a substrate.¹³ Several deficiencies in the final film stem from problems in the film-formation process. For instance, film cracking results from the buildup of capillary stresses during drying.¹⁴ Water can be trapped in drying films because of a coalesced surface layer, usually called a “skin.”¹⁵ Nanovoids in the film, which allow the transport of permeants, arise from halted or irregular patterns of particle deformation.¹⁶ Low gloss is associated with an incomplete flattening of particles at the film surface.

Although film formation is usually described in stages, the sequence of events in the structural evolution is continuous and

can overlap in time. For instance, there is experimental evidence that polymer chains interdiffuse at contact points between particles in the presence of water before particle deformation is complete.¹⁷ The various processes can also influence each other. For instance, polymers can be softened by the presence of dissolved water¹⁸ so that the rates of deformation and interdiffusion decrease as drying proceeds.¹⁹ Of interest to this present research, the particle deformation and interdiffusion processes during coalescence in a film can have a profound influence on the drying process.

Following decades of debate in the scientific literature, a consensus has emerged on the operative mechanisms for the deformation of colloidal particles during film formation. Deformation can be driven by a reduction of the interfacial energy of the particles.²⁰ If the particles are still drying such that they have an interface with water, then the process is called wet sintering. However, if drying is complete, then there is a polymer/air interface, and the process is called dry sintering.

Received: June 16, 2014

Revised: July 24, 2014

Published: July 24, 2014

Additionally, a negative capillary pressure arising from the water meniscus between particles compresses the particles in a so-called capillary deformation mechanism.²¹ Thus, the operative deformation mechanism obviously depends on the presence or absence of water.

A consideration of the relative times for the two key processes of drying and particle deformation is at the core of a model developed by Routh and Russel.²² They defined a dimensionless control parameter, $\bar{\lambda}$, as the ratio of the characteristic time for viscous particle deformation, τ_{def} , to the characteristic time for film drying, τ_{dry} . When the particle deformation time is short relative to the drying time, $\tau_{\text{def}} \ll \tau_{\text{dry}}$, then $\bar{\lambda}$ is small and particles undergo wet sintering. In the opposite case where, $\tau_{\text{def}} \gg \tau_{\text{dry}}$, then $\bar{\lambda}$ is large and particles undergo dry sintering. Capillary deformation is predicted to dominate at intermediate values of $\bar{\lambda}$. Thus, a particular latex can undergo film formation by any number of mechanisms, depending on the material properties and film-formation conditions that determine $\bar{\lambda}$. From standard sintering models,²⁰ the characteristic time for a particle of radius R_p to deform by viscous flow is proportional to its zero-shear rate viscosity, η , which resists deformation, and is inversely related to the relevant interfacial tension, γ , which drives deformation. The characteristic time for drying is proportional to the thickness, H , of the initial wet film and inversely related to the evaporation rate, \dot{E} . (Here, \dot{E} is expressed as the velocity at which the water surface falls during evaporation.) Following this argument, a definition for $\bar{\lambda}$ is apparent:

$$\bar{\lambda} = \frac{\tau_{\text{def}}}{\tau_{\text{dry}}} = \frac{\eta R_p / \gamma}{H / \dot{E}} = \frac{\eta R_p \dot{E}}{\gamma H} \quad (1)$$

The polymer viscosity, η , increases by several orders of magnitude as the temperature decreases toward the polymer's glass-transition temperature. Similarly, depending on the environmental conditions, e.g., humidity and air flow, \dot{E} can vary by more than an order of magnitude.

The distribution of particles in the vertical direction of a film (normal to the substrate) is an additional factor linked to the operative deformation mechanism. It depends on the relative rates of the particles' Brownian diffusion, which reduces any concentration gradients, and evaporation, which accumulates particles near the receding water meniscus. If evaporation is more rapid than diffusion, then particles will accumulate at the air/water interface as the particles are swept up faster than they can diffuse away. The relative importance of the two competing processes is described by a Peclét number, Pe , which is the ratio of the characteristic time of particle diffusion, τ_{diff} , to the characteristic time of drying, τ_{dry} .²² In the dilute limit, the diffusion coefficient of a spherical particle in a liquid with a viscosity μ is given by the Stokes-Einstein equation as

$$D_o = \frac{kT}{6\pi\mu R_p} \quad (2)$$

where k is the Boltzmann constant and T is the temperature. Then Pe is written as

$$Pe = \frac{\tau_{\text{diff}}}{\tau_{\text{dry}}} \approx \frac{H^2/D_o}{H/\dot{E}} = \frac{H\dot{E}}{D_o} = \frac{6\pi\mu R_p H \dot{E}}{kT} \quad (3)$$

Experiments^{23–26} and modeling²⁷ have found Pe to correlate with the vertical distribution of particles. Cardinal et al.²⁵ also considered the effects of sedimentation, in addition to evaporation and diffusion, for cases where the particles are significantly denser than the continuous medium.

In Routh and Russel's model, under conditions where $Pe \gg 1$ such that particles accumulate near the top interface, skin formation is predicted when $\bar{\lambda}$ is sufficiently low such that the particles are prone to coalescence in the presence of water via wet sintering. That is, a combination of heterogeneous drying and "soft" particles is predicted to be necessary for a skin layer to develop during film formation. Routh and Russel created a map to show the dominant deformation mechanisms determined by the particular values of $\bar{\lambda}$ and Pe .²²

Although the Routh-Russel deformation model was developed more than 15 years ago, a comprehensive and quantitative test of it is lacking. In a first attempt, Routh and Russel reviewed the literature.²⁸ They deduced the mechanism of particle deformation from qualitative descriptions of film formation and estimated values of $\bar{\lambda}$ from the experimental conditions that were reported. There was broad agreement with the model. More recently, Gonzalez et al.²⁹ varied the conditions of film formation (E and T) and the material and film parameters (R_p , η_0 , and H) to map out a wide range of $\bar{\lambda}$ values. They inferred the particle deformation mechanisms from microscopy and visual observations. There was qualitative evidence that the deformation mechanism of a particular latex was adjusted from wet sintering to capillary deformation to dry sintering as $\bar{\lambda}$ was increased. Many studies of film formation rely on visual observation to deduce the extent of drying and particle deformation.³⁰ There are also numerous studies of water loss in polymer colloids using gravimetric techniques.^{31,32} To provide more definitive data in this work, we use noninvasive nuclear magnetic resonance (NMR) profiling to study the water distribution during film formation in different regions on the Routh-Russel deformation map.

Although the film-formation research community appreciates that a skin layer will reduce the rate of water loss from polymer colloid films, the problem has not yet been systematically studied within the framework of the Routh-Russel deformation model. In this work, the value of the deformation control parameter, $\bar{\lambda}$, was varied over a wide range by adjusting the polymer viscosity via the polymer T_g in relation to the processing temperature, T . The experiments enable a careful study of the conditions leading to the growth of a skin layer. Oil-in-water emulsions exhibit an analogous variation in coalescence with position during drying.³³ This present research is motivated by a desire to identify and understand the environmental conditions and the system parameters that lead to skin formation. In the film formation of coatings, inks, and adhesives, the usual objective is to avoid the phenomenon.

MATERIALS AND METHODS

Materials. Methyl methacrylate (MMA) and butyl acrylate (BA) monomers were used as received (Acros Organics, 99% purity). Diethyl sodium sulfosuccinate (DSS), sold as Aerosol OT-75 (Cytec), was used as an emulsifier. Nonionic surfactants were excluded because they are known to have a plasticizing effect on acrylic copolymers. Ammonium persulfate (APS) (Fisher Scientific, U.K.), also known as ammonium peroxodisulfate, was used as an initiator. Deionized (DI) water was used for all experiments.

Synthesis of Acrylic Latexes by Emulsion Polymerization. Several latexes with similar average particle sizes and different glass-

transition temperatures (T_g) were synthesized using semicontinuous emulsion polymerization under monomer-starved conditions on a 1 kg scale. A 2 L reaction flask equipped with a condenser, nitrogen inlet, thermocouple linked to an electronic temperature controller and heating mantle, and anchor stirrer were employed. All ingredients in the formulation were kept the same in all polymerization reactions with the exception of the monomer ratio, which was used to adjust the polymer T_g . An example of the formulation is shown in Table 1.

Table 1. Formulation Used for the Synthesis of Latex with a T_g of 4 °C

material	quantity (g)
DI water	590
DSS	10
MMA	160
BA	240
APS	2

The reaction flask (with stirrer, nitrogen, and cooling water turned on) was charged with the surfactant and 560 g of water and was then placed in a thermostatically controlled heating mantle and allowed to reach a reaction temperature of 80 °C. MMA and BA monomers with a combined mass of 400 g were mixed, and then 1.25 wt % of this monomer mixture was added to the reactor over 3 to 4 min via a peristaltic pump while stirring at 250 rpm. A solution of APS was added to initiate the polymerization. The reaction was left for 5 min (the seed stage), after which the remaining monomer was added via a peristaltic pump over a duration of 4 h. On completion of the monomer feed, the reaction was left for an hour under the thermostatically controlled heating mantle to complete the conversion of monomers. The heating mantle was removed, and the reaction was left until the exotherm had decayed, after which the latex was cooled to room temperature and filtered using an 80 μm mesh. The average particle diameters and dispersity index, \bar{D} , were determined by dynamic light scattering using a Malvern Zetasizer Nano S, and the solids weight fractions were determined by gravimetry. Midpoint T_g values of the dried polymer were obtained by DSC analysis (Netzsch DSC 200F3) at a heating rate of 20 °C/min. The physical characteristics for a series of four latexes with differing T_g values are listed in Table 2. The mean particle sizes are nearly the same for the four latexes in the series.

Table 2. Latex Physical Characteristics

latex	monomer weight ratio (MMA:BA)	particle size, $2R_p$ (nm)	\bar{D}	T_g (°C)	solids content (wt %)
A1	17:83	63	0.08	-22	39.6
A2	30:70	60	0.09	-11	38.7
A3	40:60	71	0.03	4	39.0
A4	50:50	66	0.12	19	39.4

Surface Tension. The surface tension, γ , of the wet latexes was measured by the pendant drop test method at ambient temperature and humidity. A 5 μL pendant drop of latex was formed at the end of the capillary needle, and the images were tracked by a high-speed video system with adapter and CCD camera (up to 50 images/s digitizing speed) and analyzed by DataPhysics OCA 35 (DataPhysics Instruments, Filderstadt, Germany) using SCA20 software.

Shear Flow Viscosity. Rheological measurements were conducted using a shear rheometer (Kinexus Pro+, Malvern Instruments, U.K.) equipped with two parallel plates (top plate 20 mm in diameter). The latex samples were cast and dried in a silicone mold in open air at ambient temperature and RH for a minimum period of 72 h. A dry latex sample (with $T_g = -11$ °C) of 20 mm diameter and with a thickness of 1 mm was placed between the parallel plates. The sample temperature was first increased to 50 °C to equilibrate the sample, thus

ensuring effective contact with the parallel plates, and then reduced to the test temperature. Measurements of viscosity, η , were performed in a shear flow experiment at a constant shear rate of 10^{-3} s⁻¹ at two different temperatures of $T = 30$ and 50 °C. The viscosity was measured over a period of 1 h, during which time the viscosity approached a plateau value, which was used in subsequent analysis. As an independent check on these results, oscillatory shear measurements were also performed on the same latex at three different temperatures. The viscosity in the low-frequency limit (10⁻³ Hz) differed from the plateau viscometry measurements by a factor of 2, which is within the uncertainty of the measurements. In the calculations of the $\bar{\lambda}$ parameter, the temperature dependence of the viscosity was modeled using the Williams–Landel–Ferry (WLF) equation^{34,35} with T_g as the reference temperature

$$\eta = \eta_g \exp \left[\frac{-34(T - T_g)}{80 + T - T_g} \right] \quad (4)$$

where η_g is a prefactor for that reference temperature. Equation 4 was used to calculate the viscosity for the other latexes in the series using the same prefactor.

Atomic Force Microscopy (AFM). Latex films were cast onto glass coverslip substrates and dried under ambient conditions. AFM was performed in intermittent contact mode on a commercial microscope (NTEGRA, NT-MDT, Moscow, Russia) using silicon cantilevers (NSG01, NT-MDT) with a spring constant in the range of 1–15 N/m, a nominal resonance frequency of 138 kHz, and a tip-curvature radius of 10 nm to obtain images of latex surfaces in air. Several images of 2 μm × 2 μm areas were scanned to obtain the topographical height and corresponding phase images. For a scan of length L tracing across a sample surface, the root-mean-square (rms) roughness is calculated as

$$\text{rms}^2 = \frac{1}{L} \int_0^L (z(l) - z_0)^2 dl \quad (5)$$

where $z(l)$ is the height as a function of the position, l , and z_0 is the mean height.^{36,37}

Sample Holders for Drying Experiments. Following the method used by Trueman et al.,³⁸ drying measurements using gravimetry and GARField nuclear magnetic resonance (NMR) profiling were performed on thin glass coverslips with a laminated basin. Borosilicate glass coverslips (18 mm × 18 mm, obtained from Fisher Scientific UK) were cleaned of any contaminants by rinsing with acetone and then were placed in an ultraviolet (UV) ozone cleaner (Procleaner, Bioforce Nanosciences) with an emitting wavelength of 233 nm for up to 15 min. A wad punch (12 mm diameter) was used to cut holes in a laminate sheet that was then attached to the clean glass. A desired volume of the wet latexes was cast into the laminated basins using a micropipette (Eppendorf, 10–100 μL) and spread in the circular area of the basin (113.1 mm²). All latexes in our experiments were able to form a film at the drying temperature ($T = 22 \pm 1$ °C) as observed visually, meaning that the films were crack-free and optically transparent.

Water Loss Measurements. The loss of water from latex films was measured gravimetrically under controlled relative humidity and temperature using a digital balance (Mettler Toledo, SAG204) with a resolution of 0.1 mg, which was interfaced with a personal computer to record the readings. Prior to the measurements, the latexes were diluted with DI water to a solids content of ca. 20 wt %. The balance was placed within an environmental chamber for which the relative humidity (RH) was regulated by using saturated salt solutions. Target constant RH values of 20, 45, and 73% were achieved using saturated solutions of lithium chloride, potassium carbonate, and sodium chloride, respectively. Thirty microliters of latex was cast into the laminated basin and spread over the predetermined surface area of the glass slide. The sample mass was recorded every 2 or 5 s until there was no significant change in the value, indicating the completion of drying.

GARField NMR Profiling. Measurements of the distribution of water in the drying latex films in the direction normal to the substrate (z direction) were obtained by NMR ^1H profiling using a gradient at a right angle to the field (GARField) magnet. The design of the GARField magnet has been described elsewhere.^{39,40} The latex sample in a laminated basin was placed horizontally between the curved pole pieces above the radio-frequency (rf) coil used to excite and detect the NMR signal, as is shown in Figure 1. There is a static magnetic field

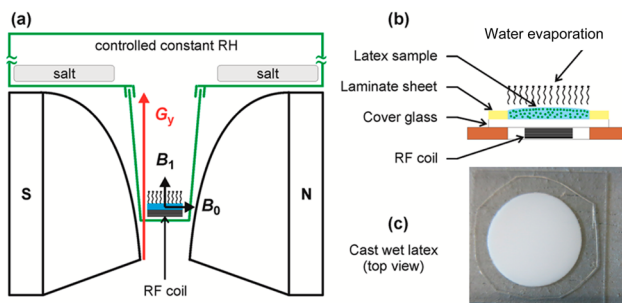


Figure 1. Schematic representation of the GARField experimental setup. The diagram on the left (a) shows shaped pole pieces that produce a strong magnetic field gradient in the vertical direction G_y and a horizontal magnetic field B_0 with a constant magnitude in the plane where the sample is placed. The coil placed underneath the sample produces an rf excitation field B_1 . The large box (shown in green) controls the RH using saturated salt solutions. The upper right side (b) shows a schematic diagram of latex cast on a basin made from a laminated glass coverslip. At the lower right (c), a photograph of latex drying in the basin is shown in a top view.

strength of $B_0 = 0.7$ T in the horizontal direction parallel to the sample plane and a magnetic field gradient strength of 17.5 T m $^{-1}$ in the direction perpendicular to the sample plane.⁴¹ The resonance condition is obtained in the sample volume at a spectrometer frequency of 28.4 MHz. Excitation field B_1 is produced by the rf coil, and it is perpendicular to the sample plane. The signal was obtained using a quadrature echo sequence: $((90x\tau-90y\tau-\text{echo}-\tau)_n\text{-RD})_{\text{NS}}$ ²⁴ and the following settings: number of echoes $n = 32$, pulse gap $\tau = 74.0$ μs , dwell time DW = 1 μs , number of points per echo SI = 128, and repetition delay RD = 2 s; NS = 128 echo trains were recorded and averaged to obtain an acceptable signal-to-noise ratio. To obtain a profile, the individual echoes in the echo train were Fourier transformed (FT) and then summed, thus giving an NMR signal intensity profile as a function of the vertical position. The intensity is proportional to the density of mobile ^1H and was therefore used to determine the distribution of water through the vertical height of the latex during drying in real time. The pixel resolution in these experiments was equal to ca. 10 μm . To correct for the decline in the sensitivity over the film thickness, the profile intensities were normalized by an elastomer standard.

In all experiments, the latex films were exposed to a controlled temperature and RH in a simple setup having two closed spaces of different volumes (Figure 1). A removable box with a significantly larger volume has an RH value maintained at equilibrium with saturated salt solutions (as were likewise used in the gravimetric measurements). This box was placed on top of the magnet and connected to a second smaller space that was located between the magnet poles surrounding the drying sample. Because of the significant difference in the volumes, the small fluctuations of RH during placing or changing the sample are quickly equilibrated, thus allowing tight control of RH for the duration of the experiment.

RESULTS AND DISCUSSION

Effect of Latex Polymer T_g on Rates of Water Loss. We first consider measurements of the water loss for the series of four latexes obtained using gravimetric analysis. Figure 2 shows

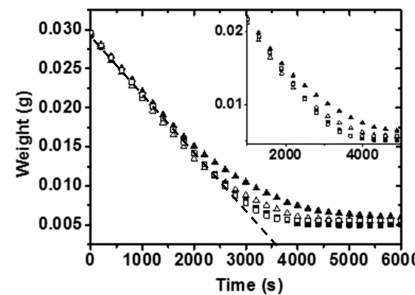


Figure 2. Mass loss as a function of time for the latex series with various values of T_g : -22 (\blacktriangle), -11 (\triangle), 4 (\blacksquare), and 19 $^\circ\text{C}$ (\square), when drying under an ambient temperature of 22 ± 1 $^\circ\text{C}$ in still air with $\text{RH} = 43 \pm 2\%$. The dashed line shows the initial constant rate of water loss prior to the falling rate period.

the evolution of the mass over time in latexes with four different T_g values when held at a controlled constant temperature (22 ± 1 $^\circ\text{C}$) and RH ($43 \pm 2\%$) in still air. In these experiments, the initial wet films had the same thickness, surface area, and solids content. For all four latexes, there is an initial constant rate of water loss that takes the same value for each, 6.8×10^{-6} g cm $^{-2}$ s $^{-1}$, which is comparable to what has been reported in the literature for pure water (cf. 5×10^{-6} g cm $^{-2}$ s $^{-1}$ for Tsuji et al.⁴² and 4×10^{-6} g cm $^{-2}$ s $^{-1}$ (at 50% RH) for Rösler et al.⁴³). In this first period, the water loss rate is set by the free evaporation rate of water. After about 2500 s, this constant rate period is followed by a falling rate period in which the rate of water loss is seen to slow down. The falling rate is determined by the transport of water around or through the bed of polymer particles.³² It can be observed that as the T_g of the latex is reduced (and as $T-T_g$ is increased), the rate of water loss slows down. After 4000 s, the mass reaches a constant value that indicates the completion of drying and defines a drying time, t_{dry} . For these films with the same thickness, surface area, and solids content, the drying time increases as the T_g of the latex decreases. This result indicates that the polymer particles have an effect on the falling rate period of drying. To understand and to explain this result, we determined the distribution of water in the latex films in the vertical direction during drying using the GARField NMR technique.

The NMR signal intensity is proportional to the concentration of water in the films at a particular position. The drying time for a latex film corresponds to the point at which the NMR signal intensity reaches zero or a baseline value (in cases where there is a signal from the polymer phase). (See Supporting Information, Figure S1.) For polymers with the lowest T_g of -22 $^\circ\text{C}$, the molecules have sufficient mobility at room temperature to produce an NMR signal with the experimental parameters used; hence, the polymer phase contributes to the total signal throughout the measurement. Figure 3 shows the GARField profiles of this latex when drying under an RH of 73%. The position of 0 represents the interface of the film with the substrate. The top of the wet film is initially at a height of ca. 450 μm . For the first 300 min of drying, the profiles are flat, indicating a uniform concentration of water throughout the depth of the film. Thereafter, a step in the profile develops near the film's interface with the air, and there is a higher concentration of water near the substrate. A top surface layer with a negligible water content develops and grows thicker over time. We refer to this surface layer hereafter as a skin. A water gradient remains in the film until the latest

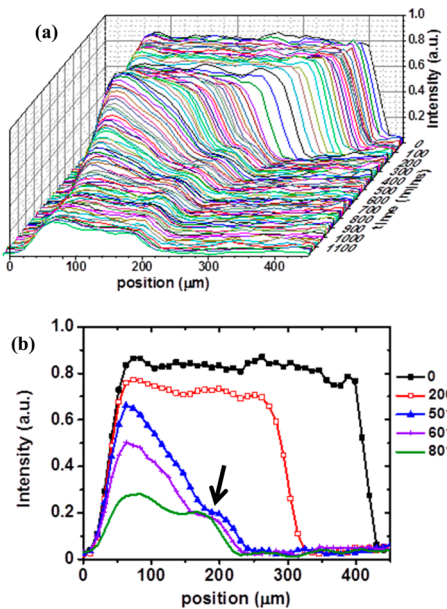


Figure 3. GARField NMR profiles for latex with a T_g of $-22\text{ }^\circ\text{C}$ drying at a temperature of $22 \pm 1\text{ }^\circ\text{C}$ and a relative humidity of $73 \pm 2\%$. (a) Profiles are shown throughout the process with time presented on the third axis. (b) Selected profiles are shown at selected times (min) given in the legend. A step in the water concentration is found during times starting at approximately 500 min. The arrow points to the region interpreted to be the skin layer. An analysis of the NMR intensity loss finds $t_{\text{dry}} = 980$ min. For this experiment, $\bar{\lambda} = 3.2 \times 10^{-4}$ and $Pe = 1.9$.

stages of drying. The NMR signal intensity decreases until a time of 980 min, which defines the drying time. Similar water profiles were reported by Rodriguez et al. in blends of acrylic latex and poly(dimethylsiloxane) (PDMS) emulsion with a T_g of $-127\text{ }^\circ\text{C}$ when drying at room temperature.⁴⁴ They attributed the skin formation to the coalescence of the PDMS droplets near the film surface.

Next, the evolution of water concentration profiles is considered under identical environmental conditions for the latex with a T_g of $-11\text{ }^\circ\text{C}$ (Figure 4). As in the previous experiment, the water concentration is initially uniform in depth. Linear gradients develop at later stages of drying, starting from about 200 min. Unlike what was seen for the latex with a T_g of $-22\text{ }^\circ\text{C}$, there is no step in the profile associated with a skin layer. The decrease in the NMR signal stops at a drying time of $t_{\text{dry}} = 616$ min.

Next, a latex with a T_g closer to the temperature of film formation is considered. Figure 5 shows NMR profiles obtained from the latex with a T_g of $4\text{ }^\circ\text{C}$. In this case, the profiles remain rather square throughout the drying process and exhibit only a slight gradient in the final stages of drying. The water concentration is only slightly lower near the film/air interface. Notably, the water is fully lost from the film (as is indicated by the loss of the NMR signal) after 247 min. With $T_g = 19\text{ }^\circ\text{C}$, the GARField NMR profiles show that the water concentration is uniform with depth throughout the films (Supporting Information, Figure S1), and there is no gradient in water concentration.

In summary, the water distribution in the vertical direction during latex film formation shows a strong function of the T_g of the polymer when the other parameters are not varied. At the lowest T_g ($-22\text{ }^\circ\text{C}$), there is a step in the water concentration,

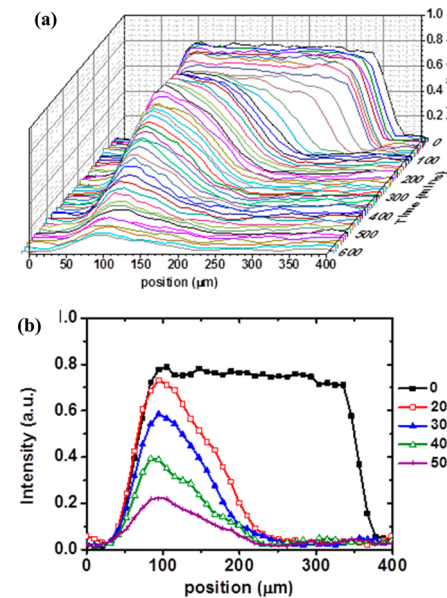


Figure 4. GARField NMR profiles for a latex with a T_g of $-11\text{ }^\circ\text{C}$ at a temperature of $22 \pm 1\text{ }^\circ\text{C}$ and a relative humidity of $73 \pm 2\%$. (a) Profiles are shown throughout the process with time presented on the third axis. (b) Selected profiles are shown at selected times (min) given in the legend. From approximately 200 min, a linear concentration gradient of water is observed, and the gradient decreases as drying proceeds. An analysis of the NMR intensity loss finds $t_{\text{dry}} = 616$ min. For this experiment, $\bar{\lambda} = 3.3 \times 10^{-3}$ and $Pe = 1.4$.

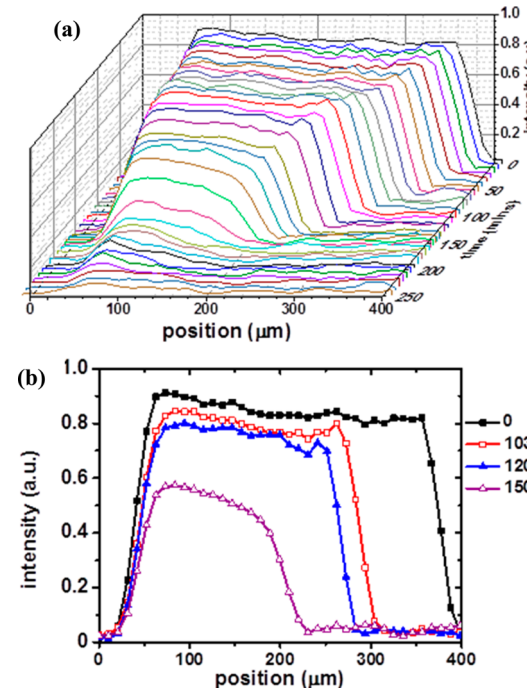


Figure 5. GARField NMR profiles for latex with a T_g of $4\text{ }^\circ\text{C}$ drying at a temperature of $22 \pm 1\text{ }^\circ\text{C}$ and a relative humidity of $73 \pm 2\%$. (a) Profiles are shown throughout the process with time presented on the third axis. (b) Selected profiles are shown at selected times (min) given in the legend. An analysis of the NMR intensity loss finds $t_{\text{dry}} = 247$ min. For this experiment, $\bar{\lambda} = 1.2 \times 10^{-1}$ and $Pe = 1.9$. The profiles are relatively square throughout the drying process, with only a slight water concentration gradient.

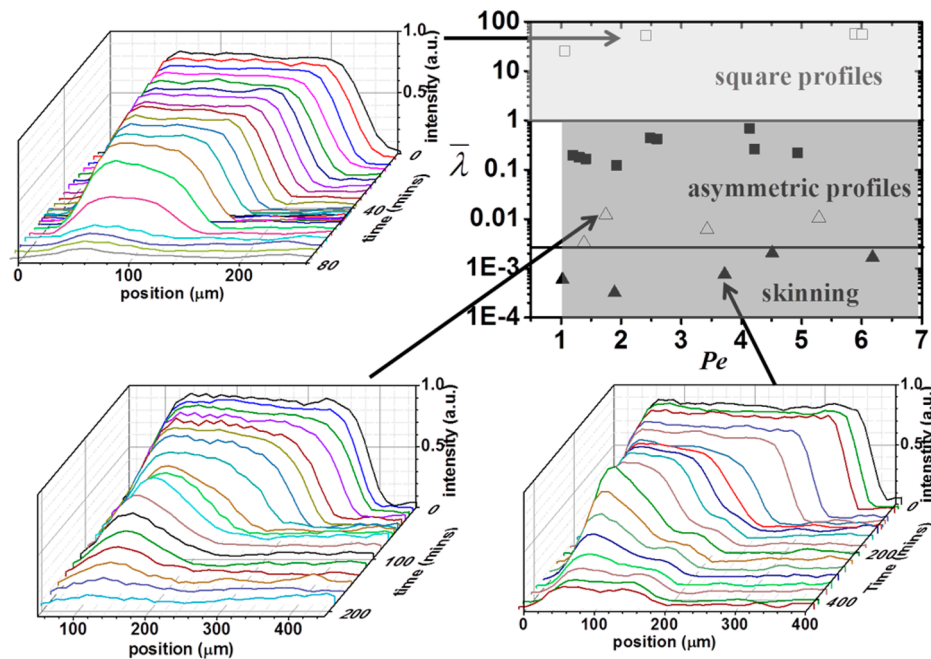


Figure 6. Deformation map of latexes for all experiments with T_g values of -22 (\blacktriangle), -11 (\triangle), 4 (\blacksquare), and 19°C (\square) and GARField nuclear magnetic resonance profiles exhibiting different drying characteristics obtained at a temperature of $22 \pm 1^\circ\text{C}$ and RH of $43 \pm 2\%$. Representative GARField profiles are shown with different characteristics: square profiles (upper left side, $T_g = 19^\circ\text{C}$); asymmetric profiles (bottom left, $T_g = -11^\circ\text{C}$); and skinning (bottom right, $T_g = -22^\circ\text{C}$). The shading in the deformation map identifies the regimes predicted by the Routh–Russel model: capillary deformation in light gray, skin formation in dark gray, and wet sintering without skin formation in white.

indicative of a dry skin layer near the film's interface with air. At an intermediate T_g (-11°C), linear concentration gradients place the lowest water concentration at the air interface. At the highest T_g (4°C), the water concentration varies only slightly with distance from the air interface. Water is distributed more uniformly in the vertical direction. As was also found in the gravimetry experiments, the drying times obtained from the NMR experiments decreased as the polymer's T_g increased. The trend is apparent in the data in Figure S2 (Supporting Information). In the next section, we will explain these results by considering particle deformation.

Application of the Routh–Russel Model to the Experimental Results. To explain the large differences in the water concentration profiles as the polymer T_g is varied, the Routh–Russel model is now employed. The model uses two dimensionless parameters, Pe and $\bar{\lambda}$, as were stated in eqs 1 and 3. The values of Pe and $\bar{\lambda}$ are determined by characteristics of the colloidal dispersion (R_p , η , μ , and γ) and by the film-formation process parameters (H , E , and T). In turn, the polymer viscosity, η , is a strong function of the temperature used in the process in relation to the polymer's T_g (eq 4). In our experiments, all of the parameters used in Pe and $\bar{\lambda}$ were found in independent measurements or taken from the literature, as described hereafter.

Gravimetric measurements of water loss from latex films under two different environmental conditions (for example, Figure S3, Supporting Information) were used to find the evaporation rates at the start of the process. The best fit to the initial linear region was used to measure the change in mass (m) with time (t), (dm/dt) . For each experiment, E (a velocity) was calculated from $(dm/dt)(1/\rho A)$, assuming the density of water to be $\rho = 1 \text{ g cm}^{-3}$ and using the measured surface area, A , of the cast latex in the laminated basin (1.13 cm^2).

The average radii of the particles, R_p , as obtained by dynamic light scattering are listed in Table 2. The water–air surface tension, γ , was measured by the pendant drop method on several latexes and found to be 48 mN/m . The viscosity (μ) of the continuous phase of the wet latex at room temperature is taken to be the value of water: $\mu = 1.00 \text{ mPa s}$. The initial wet film thickness, H , was measured from the width of the first GARField profile, obtained immediately after casting the film. The top and bottom edges of the profiles were defined by the positions with a normalized signal intensity of 0.1. (Supporting Information, Figure S4.)

The variable that has the greatest effect on the value of $\bar{\lambda}$ is the low shear viscosity of the polymer, η . This parameter was measured directly for thick layers of latex A2 at two temperatures (30 and 50°C), which are above the polymer's T_g of -11°C (Supporting Information, Figure S5.) Using eq 4, we obtained a value of $\eta_g = 1.3 \times 10^{12} \text{ Pa s}$ (mean value for the two test temperatures) from the plateau value of viscosity. This value was subsequently used to calculate η at room temperature for the latex series having a range of T_g values.

In our experiments, Pe was adjusted by varying E and the initial thickness of the latex, H . Additionally, $\bar{\lambda}$ was adjusted by varying η by using a range of polymer T_g values. The Pe and $\bar{\lambda}$ values corresponding to all of the GARField NMR experiments are presented in Figure 6 in the form of a Routh–Russel deformation map. In the majority of experiments, $Pe \gg 1$, which means that nonuniform water distributions during drying are expected. The map is shaded to designate the regimes predicted by the Routh–Russel model.^{22,28} Capillary deformation is predicted when $10^2 > \bar{\lambda} > 1$ (shown in light gray on the map). Skin formation is predicted when $Pe > 1$ and $\bar{\lambda} < 1$ (dark gray). Wet sintering (without skin formation) is predicted when $Pe < 1$ and $\bar{\lambda} < 1$ (white). We attempted to access the dry sintering regime ($\bar{\lambda} > 10^2$) in our experiments, but the

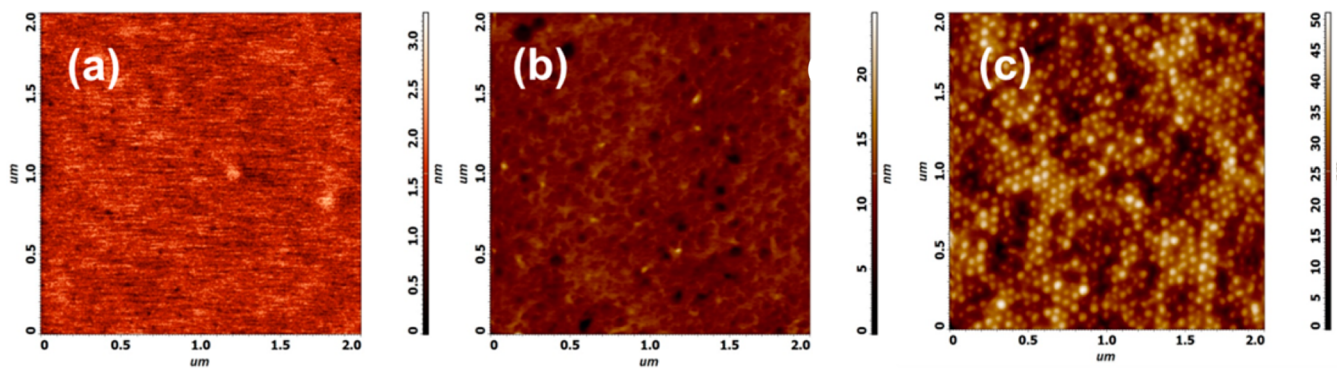


Figure 7. AFM height images of latex film surfaces ($2 \mu\text{m} \times 2 \mu\text{m}$ areas) after film formation at room temperature, comparing polymers with different T_g values: (a) -22 , (b) 4 , and (c) 19 $^{\circ}\text{C}$.

acquisition of reliable NMR profiles was hindered by film cracking and delamination.

Representative NMR profiles are presented in different regions of the map. Square profiles (indicating homogeneous drying through the vertical height of the film) were found experimentally with $\bar{\lambda} > 1$ in the capillary deformation regime. If the deformation of the particles under capillary pressure is uniform through the depth of the film, then a uniform concentration of water (exhibiting square profiles) is expected. The results agree with the model.

Asymmetric linear profiles were found in the region of the map where $0.02 < \bar{\lambda} < 1$, which is in the wet sintering and skin formation regime in the model. Profiles exhibiting skin formation (indicated by a discrete, dry surface layer) are found in the region of the map where $\bar{\lambda} < 0.02$. This pronounced skin formation, with a well-defined surface layer, was observed as the polymer viscosity was reduced by increasing the quantity $T - T_g$. We conclude that skin formation occurs in the region that is predicted by the model, although a discrete skin layer is not observed until $\bar{\lambda}$ is sufficiently low (<0.02).

The parameters found in the deformation map indicate that the latex with a T_g of -22 $^{\circ}\text{C}$ will undergo wet sintering, which means that particle deformation takes place in the presence of water. The relatively high Pe is expected to lead to a nonuniform water distribution and the formation of a skin layer. AFM analysis of this latex film (Figure 7a) shows that individual particle identity at the air interface has been lost. A surface roughness of only 0.3 nm indicates that the particles have flattened and lost their identity. The surface structure is what would be expected for a coalesced surface. By comparison, when the T_g is 19 $^{\circ}\text{C}$, the model predicts capillary deformation. AFM analysis of the film surface (Figure 7c) reveals domelike particles at the air interface with some nanovoids between particles; the rms roughness is 7.1 nm. This open structure would be permeable to water. (The images were obtained after 5 days of aging at room temperature and ambient RH. Hence, some particle flattening and coalescence would have taken place during that period.) An intermediate structure is found for the latex with a T_g of 4 $^{\circ}\text{C}$ (Figure 7b). Some remnant particle structure is observed, as explained by partial coalescence.

The Routh–Russel model does not explicitly predict the water distribution during the later stages of film formation. However, Narita et al. made predictions of water profiles when water was undergoing flow through a packed bed of particles.³² Routh and Russel noted that skin formation will reduce the rate of water loss because the diffusion of water through a coalesced

film is slow relative to transport by Darcy flow through a bed of packed particles.²²

With the aim of identifying the reasons for the slowing of drying rates in a softer latex, we next explore the extent to which the deformation control parameter, $\bar{\lambda}$, correlates with the film drying time. As our experiments used a range of film thicknesses, temperatures, and relative humidities, absolute drying times cannot be compared. Instead, a dimensionless drying time, t_{dry}^* , is calculated by dividing the experimental t_{dry} by the drying time predicted from the initial free evaporation

rate, $H(1 - \phi)/E$, where ϕ is the initial solids volume fraction. When the water loss rate slows during the drying process, t_{dry}^* will be greater than unity. Thus, t_{dry}^* can be taken to be a simple measure of the extent of drying impediment, such as by skin formation.

Figure 8 shows how the dimensionless drying time, t_{dry}^* varies with $\bar{\lambda}$. The black data points represent experiments

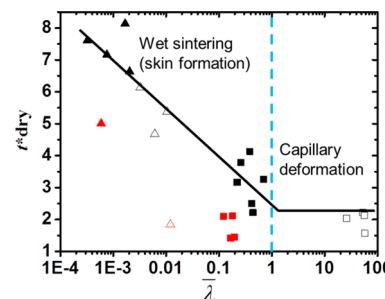


Figure 8. Variation of normalized drying time, t_{dry}^* , against $\bar{\lambda}$ for latexes with T_g values of -22 (\blacktriangle), -11 (\triangle), 4 (\blacksquare), and 19 $^{\circ}\text{C}$ (\square). Outliers with red symbols are for thin films ($180 < H < 270 \mu\text{m}$) with a lower Peclét number ($1 < Pe < 2$). All other points are for thicker films ($270 < H < 409 \mu\text{m}$). The trendline follows $t_{\text{dry}}^* = 2.5 - 1.5 \log \bar{\lambda}$.

where $Pe > 2$. For this regime, the data show that when $\bar{\lambda}$ is reduced to below 1, longer drying times result. Up to a value of $\bar{\lambda} = 1$, there is broadly an inverse correlation between t_{dry}^* and $\bar{\lambda}$, given by a line of best fit: $t_{\text{dry}}^* = 2.5 - 1.5 \log \bar{\lambda}$. Physically, this represents an increase in the drying time by a multiple of the free evaporation time when decreased by approximately 1 order of magnitude.

It is seen that increasing $\bar{\lambda}$ to above 1 has no effect on the drying times. This transition point at $\bar{\lambda} = 1$ corresponds to the onset of capillary deformation where the particles are deformed at the same rate at which water is lost. The interparticle void spaces (created by Plateau borders⁵) remain open during

drying, and there is only a slight impediment to water evaporation in comparison to free evaporation. In this regime, t^*_{dry} is expected to be on the order of unity, as is observed experimentally.

When $\bar{\lambda}$ decreases and lies within the range for wet sintering, the dimensionless drying times are seen to become exceedingly long (>8). When $Pe > 1$, this regime corresponds to skin formation and an associated impediment to evaporation. Hence, the long drying times found in our experiments are well explained by the model. When $\bar{\lambda}$ is decreased farther into the wet sintering regime, the skin formation and the extent of the slowing of the drying become stronger.

The red data points in Figure 8 were obtained from thinner films ($H \ll 270 \mu\text{m}$) and/or at lower evaporation rates ($\text{RH} = 75 \pm 2\%$) under conditions leading to $Pe < 2$. Slowing the evaporation rate allows enough time for the particles to diffuse in the vertical direction of the film, hence encouraging a homogeneous water concentration. As a general trend, t^*_{dry} is lower in these experiments with $Pe < 2$, when particles will be more uniformly distributed in the vertical direction, with a shallower concentration gradient.²⁷ Thus, the experiments find a weaker slowing down of drying when the tendency toward skin formation is weaker.

The results in Figure 8 demonstrate clearly that although a large number of parameters influence the latex film formation process, the use of dimensionless parameters shows useful trends that are fully consistent with the Routh–Russel model. The application of the model enables a user of latex films to select the polymer and to set the environmental conditions and film thickness appropriately to attain the fastest possible drying times. The vexing problem of slow drying caused by skin formation becomes tractable.

It is relevant to note that in polymer systems, particle deformation requires a non-negligible amount of time and is longer than the drying time in the case of dry sintering. On the other hand, in oil-in-water emulsions, the dispersed oil phase has a much lower viscosity in comparison to that of polymers, and droplet coalescence can be very fast in relation to drying. In an emulsion system, Feng et al.³³ identified the importance of the emulsion's disjoining pressure in determining the water concentration profile during drying. When the disjoining pressure was high, they observed droplet coalescence throughout the concentrated emulsion, which they called bulk coalescence. In emulsions with a low disjoining pressure, they found a mechanism of front coalescence, where coalescence moved inward from the interface with air. Front coalescence created an oil layer that impeded subsequent water evaporation. This mechanism is analogous to the skin formation observed in Figure 3. In polymer systems, such as studied in the present work, the effects of disjoining pressure are expected to be less important because the particle deformation by viscous flow is rate-controlling.

CONCLUSIONS

The Routh–Russel process model of particle deformation has been applied to well-characterized latexes over a wide range of controlled environmental conditions. It is important to highlight that the latexes were free of coalescing or wetting agents, and all the ingredients were kept the same with the exception of the monomer ratios, varied to adjust the T_g . Direct comparison was enabled by eliminating all other variables.

In systematic experiments, Pe and $\bar{\lambda}$ were adjusted by changing the wet film thickness, H , the evaporation rate, E , and the polymer viscosity, η , through the variation of T_g . The drying times for films of identical thickness and atmospheric conditions were found to be inversely related to T_g . Water concentration profiles in the vertical direction in the film were obtained throughout the film-formation process for the same series of latex. As the copolymer's T_g was reduced, linear concentration gradients developed. With the lowest T_g of -22°C , a coalesced surface layer—or skin—was evident in the concentration profiles.

Parameters were selected to access various regimes in a Routh–Russel deformation map ($\bar{\lambda}$ vs Pe). Skin layers were seen to develop when $\bar{\lambda} < 0.02$, obtained when $T - T_g$ was high ($>33^\circ\text{C}$). In this case, the skin layer resulted in drying times that were 5 to 8 times longer than expected from the free evaporation rate of water at the onset of the process. On the other hand, with $\bar{\lambda} > 1$, obtained when $T - T_g$ was small, the water concentration was more uniform with depth; there was no evidence of skin formation in the NMR profiles. Consequently, there was no slowing down of the drying process. In the low- $\bar{\lambda}$ regime, when Pe was kept small (<2), skin formation was less severe, and the decrease in the drying times was weaker.

The experimental results support the Routh–Russel model. In the capillary deformation regime ($1 < \bar{\lambda} < 10^2$), the water concentration is uniform with depth. The drying process is not significantly impeded by the deformed particles. As expected from the model, there is experimental evidence for skin formation when $\bar{\lambda} < 1$ (in the wet sintering regime) and when $Pe > 1$. In this case, drying times are longer. The dimensionless drying time, t^*_{dry} , is on the order of unity at the transition point from the wet sintering to the capillary deformation regime, where $\bar{\lambda} = 1$. Below this transition point, an inverse relation is given as $t^*_{\text{dry}} = 2.5 - 1.5 \log \bar{\lambda}$. As $\bar{\lambda}$ is decreased, the impediment to the drying rate becomes stronger.

A consideration of the effects of the various parameters leads to an important insight. Low Pe values (in order to avoid the skin-formation regime) can be achieved when the product of H and E is small. On the other hand, a high value of $\bar{\lambda}$, to avoid wet sintering and possible skin formation, is achieved when the ratio of E/H is high. Decreasing the film thickness, H , thus provides a way to avoid skin formation.

This research has indicated that the processing conditions and material parameters can be adjusted to ensure that $\bar{\lambda}$ and Pe take values outside of the wet sintering regime as a way to avoid the slow drying caused by skin formation. The model and experiments show that skin formation can be avoided with thinner films, faster initial evaporation rates (as with low humidity and flowing air), and higher polymer viscosity (as with T just slightly above T_g). The effects of the processing temperature are more difficult to predict because of competing effects. Increasing T will increase particle diffusivity and will normally increase E (depending on the humidity). The effect of T on Pe will be small and will depend on the strength of the temperature dependence of E . Increasing T will lower the polymer viscosity, η , and thereby decrease $\bar{\lambda}$ toward the wet sintering regime. However, the effects can be counterbalanced if the increase in E is sufficiently large.

■ ASSOCIATED CONTENT

● Supporting Information

GARField NMR profiles during the film formation of the latex with a T_g of 19 °C. NMR signal intensity for all four latexes during drying. Gravimetric data to determine evaporation rates at two different humidities. Measurement of film thickness from the GARField profile from a wet film. Polymer viscosity measurement at two temperatures using constant shear rheology. This material is available free of charge via the Internet at <http://pubs.acs.org>.

■ AUTHOR INFORMATION

Corresponding Author

*E-mail: j.keddie@surrey.ac.uk.

Present Address

(R.M.K.): Chemical Analytical Facility, School of Chemistry, Food and Pharmacy, University of Reading, Reading, Berkshire, RG6 6AH United Kingdom.

Author Contributions

The manuscript was written through the contributions of all authors. All authors have given approval to the final version of the manuscript.

Notes

The authors declare no competing financial interest.

■ ACKNOWLEDGMENTS

We gratefully acknowledge funding from Engineering and Physical Science Research Council (EPSRC) and AkzoNobel International Paint, Felling, U.K., for the EngD studentship of F.T.C. We thank V. Doukova (University of Surrey), G. Worrall, and D. Graham (AkzoNobel International Paint, Felling, U.K.) for experimental assistance. We are grateful to M. Murray and N. Williams (AkzoNobel, Slough, U.K.), A. F. Routh (University of Cambridge), and S. Sajjadi (King's College London, U.K.) for helpful discussions.

■ REFERENCES

- (1) Keddie, J.; Routh, A. *Fundamentals of Latex Film Formation: Processes and Properties*; Springer: Dordrecht, The Netherlands, 2010.
- (2) Russel, W. B. Mechanics of Drying Colloidal Dispersions: Fluid/Solid Transitions, Skinning, Crystallization, Cracking, and Peeling. *AIChE J.* **2011**, *57*, 1378–1385.
- (3) Visschers, M.; Laven, J.; Linde, R. van der. Film Formation from Latex Dispersions. *J. Coatings Technol.* **2001**, *73*, 49–55.
- (4) Routh, A. F. Drying of Thin Colloidal Films. *Rep. Prog. Phys.* **2013**, *76*, 46603.
- (5) Crowley, T.; Sanderson, A.; Morrison, J. Formation of Bilayers and Plateau Borders during the Drying of Film-Forming Latexes as Investigated by Small-Angle Neutron Scattering. *Langmuir* **1992**, *8*, 2110–2123.
- (6) Rharbi, Y.; Boué, F.; Joanicot, M.; Cabane, B. Deformation of Cellular Polymeric Films. *Macromolecules* **1996**, *29*, 4346–4359.
- (7) Gonzalez, E.; Tollar, C.; Chuvilin, A.; Barandiaran, M. J.; Paulis, M. Determination of the Coalescence Temperature of Latexes by Environmental Scanning Electron Microscopy. *ACS Appl. Mater. Interfaces* **2012**, *29*, 4276–4282.
- (8) Visschers, M.; Laven, J.; van der Linde, R. Forces Operative during Film Formation from Latex Dispersions. *Prog. Org. Coatings* **1997**, *31*, 311–323.
- (9) Pekcan, Ö.; Arda, E. Void Closure and Interdiffusion in Latex Film Formation by Photon Transmission and Fluorescence Methods. *Colloids Surf., A* **1999**, *153*, 537–549.
- (10) Arda, E.; Özer, F.; Pişkin, E.; Pekcan, Ö. Film Formation from Nanosized Copolymeric Latex Particles: A Photon Transmission Study. *J. Colloid Interface Sci.* **2001**, *233*, 271–279.
- (11) Kim, K. D.; Sperling, L. H.; Klein, A.; Hammouda, B. Reptation Time, Temperature, and Cosurfactant Effects on the Molecular Interdiffusion Rate during Polystyrene Latex Film Formation. *Macromolecules* **1994**, *27*, 6841–6850.
- (12) Wang, Y.; Winnik, M. A. Polymer Diffusion across Interfaces in Latex Films. *J. Phys. Chem.* **1993**, *97*, 2507–2515.
- (13) Ma, Y.; Davis, H. T.; Scriven, L. E. Microstructure Development in Drying Latex Coatings. *Prog. Org. Coat.* **2005**, *52*, 46–62.
- (14) Russel, W. B.; Wu, N.; Man, W. Generalized Hertzian Model for the Deformation and Cracking of Colloidal Packings Saturated with Liquid. *Langmuir* **2008**, *24*, 1721–1730.
- (15) Mallégol, J.; Bennett, G.; McDonald, P. J.; Keddie, J. L.; Dupont, O. Skin Development during the Film Formation of Waterborne Acrylic Pressure-Sensitive Adhesives Containing Tackifying Resin. *J. Adhes.* **2006**, *82*, 217–238.
- (16) Nawaz, Q.; Rharbi, Y. Various Modes of Void Closure during Dry Sintering of Close-Packed Nanoparticles. *Langmuir* **2009**, *26*, 1226–1231.
- (17) Pohl, K.; Adams, J.; Johannsmann, D. Correlation between Particle Deformation Kinetics and Polymer Interdiffusion Kinetics in Drying Latex Films. *Langmuir* **2013**, *29*, 11317–11321.
- (18) Tsavalas, J. G.; Sundberg, D. C. Hydroplasticization of Polymers: Model Predictions and Application to Emulsion Polymers. *Langmuir* **2010**, *26*, 6960–6966.
- (19) Soleimani, M.; Haley, J. C.; Lau, W.; Winnik, M. A. Effect of Hydroplasticization on Polymer Diffusion in Poly(butyl Acrylate-Co-Methyl Methacrylate) and Poly(2-Ethylhexyl Acrylate-Co-Tert-Butyl Methacrylate) Latex Films. *Macromolecules* **2009**, *43*, 975–985.
- (20) Dillon, R. E.; Matheson, L. A.; Bradford, E. B. Sintering of Synthetic Latex Particles. *J. Colloid Sci.* **1951**, *6*, 108–117.
- (21) Brown, G. L. Formation of Films from Polymer Dispersions. *J. Polym. Sci.* **1956**, *22*, 423–434.
- (22) Routh, A. F.; Russel, W. B. A Process Model for Latex Film Formation: Limiting Regimes for Individual Driving Forces. *Langmuir* **1999**, *15*, 7762–7773.
- (23) Chen, X.; Fischer, S.; Yi, Z.; Boyko, V.; Terrenoire, A.; Reinhold, F.; Rieger, J.; Li, X.; Men, Y. Structural Reorganization of a Polymeric Latex Film during Dry Sintering at Elevated Temperatures. *Langmuir* **2011**, *27*, 8458–8463.
- (24) Ekanayake, P.; McDonald, P. J.; Keddie, J. L. An Experimental Test of the Scaling Prediction for the Spatial Distribution of Water during the Drying of Colloidal Films. *Eur. Phys. J. Spec. Top.* **2009**, *166*, 21–27.
- (25) Cardinal, C. M.; Jung, Y. D.; Ahn, K. H.; Francis, L. F. Drying Regime Maps for Particulate Coatings. *AIChE J.* **2010**, *56*, 2769–2780.
- (26) Gorce, J.-P.; Bovey, D.; McDonald, P. J.; Palasz, P.; Taylor, D.; Keddie, J. L. Vertical Water Distribution during the Drying of Polymer Films Cast from Aqueous Emulsions. *Eur. Phys. J. E* **2002**, *8*, 421–429.
- (27) Routh, A. F.; Zimmerman, W. B. Distribution of Particles during Solvent Evaporation from Films. *Chem. Eng. Sci.* **2004**, *59*, 2961–2968.
- (28) Routh, A. F.; Russel, W. B. Deformation Mechanisms during Latex Film Formation: Experimental Evidence. *Ind. Eng. Chem. Res.* **2001**, *40*, 4302–4308.
- (29) Gonzalez, E.; Paulis, M.; Barandiaran, M. J.; Keddie, J. L. Use of a Routh-Russel Deformation Map to Achieve Film Formation of a Latex with a High Glass Transition Temperature. *Langmuir* **2013**, *29*, 2044–2053.
- (30) Jensen, D.; Morgan, L. Particle Size as It Relates to the Minimum Film Formation Temperature of Latices. *J. Appl. Polym. Sci.* **1991**, *42*, 2845–2849.
- (31) Croll, S. G. Drying of Latex Paint. *J. Coat. Technol.* **1986**, *58*, 41–49.
- (32) Narita, T.; Héraud, P.; Lequeux, F. Effects of the Rate of Evaporation and Film Thickness on Nonuniform Drying of Film-Forming Concentrated Colloidal Suspensions. *Eur. Phys. J. E* **2005**, *17*, 69–76.

- (33) Feng, H.; Sprakel, J.; Ershov, D.; Krebs, T.; Cohen Stuart, M. A.; van der Gucht, J. Two Modes of Phase Inversion in a Drying Emulsion. *Soft Matter* **2013**, *9*, 2810.
- (34) Williams, M. L.; Landel, R. F.; Ferry, J. D. The Temperature Dependence of Relaxation Mechanisms in Amorphous Polymers and Other Glass-Forming Liquids. *J. Am. Chem. Soc.* **1955**, *77*, 3701–3707.
- (35) Strobl, G. R. *The Physics of Polymers*, 2nd ed.; Springer: Berlin, 1997; Vol. 2, p 230.
- (36) Georgiadis, A.; Bryant, P. A.; Murray, M.; Beharrell, P.; Keddie, J. L. Resolving the Film-Formation Dilemma with Infrared. *Langmuir* **2011**, *27*, 2176–2180.
- (37) Pérez, E.; Lang, J. Flattening of Latex Film Surface: Theory and Experiments by Atomic Force Microscopy. *Macromolecules* **1999**, *32*, 1626–1636.
- (38) Trueman, R. E.; Lago Domingues, E.; Emmett, S. N.; Murray, M. W.; Keddie, J. L.; Routh, A. F. Autostratification in Drying Colloidal Dispersions: Experimental Investigations. *Langmuir* **2012**, *28*, 3420–3428.
- (39) Glover, P. M.; Aptaker, P. S.; Bowler, J. R.; Ciampi, E.; McDonald, P. J. A Novel High-Gradient Permanent Magnet for the Profiling of Planar Films and Coatings. *J. Magn. Reson.* **1999**, *139*, 90–97.
- (40) McDonald, P. J.; Aptaker, P. S.; Mitchell, J.; Mulheron, M. A. Unilateral NMR Magnet for Sub-Structure Analysis in the Built Environment: The Surface GARField. *J. Magn. Reson.* **2007**, *185*, 1–11.
- (41) Bennett, G.; Gorce, J.-P.; Keddie, J. L.; McDonald, P. J.; Berglind, H. Magnetic Resonance Profiling Studies of the Drying of Film-Forming Aqueous Dispersions and Glue Layers. *Magn. Reson. Imaging* **2003**, *21*, 235–241.
- (42) Tsuji, M.; Nakahara, H.; Moroi, Y.; Shibata, O. Water Evaporation Rates across Hydrophobic Acid Monolayers at Equilibrium Spreading Pressure. *J. Colloid Interface Sci.* **2008**, *318*, 322–330.
- (43) Rösler, M. A.; Klinke, E.; Kunz, G. Evaporation of Solvents by Infrared Radiation Treatment. *Prog. Org. Coat.* **1994**, *23*, 351–362.
- (44) Rodríguez, R.; de las Heras-Alarcón, C.; Ekanayake, P.; McDonald, P. J.; Keddie, J. L.; Barandiaran, M. J.; Asua, J. M. Correlation of Silicone Incorporation into Hybrid Acrylic Coatings with the Resulting Hydrophobic and Thermal Properties. *Macromolecules* **2008**, *41*, 8537–8546.